Microwave Imaging Using Noise Signals

Stavros Vakalis, Student Member, IEEE, and Jeffrey A. Nanzer¹⁰, Senior Member, IEEE

Abstract-A new method of active incoherent microwave imaging is presented that uses noise signals and spatial frequency sampling. Building on interferometric spatial frequency sampling arrays developed in radio astronomy, active incoherent microwave imaging utilizes the transmission of noise signals to implement the first active imaging method that samples in the spatial frequency domain. In comparison to passive microwave imaging systems, active incoherent imaging requires receivers with far less sensitivity, and thus less overall cost. We present the theory behind the imaging technique and show experimental results from a 5.85-GHz system imaging in one and two dimensions. For 1-D images, the transmitter consisted of two noise generators, while the receive array was a synthesized linear array with elements placed in 1λ increments with the widest spacing of 15λ. For 2-D images, the transmitter consisted of three noise generators, while the receive array was a synthesized T-array with elements placed in 0.5λ increments. We demonstrate the reconstruction of 1-D and 2-D scenes consisting of spherical reflecting targets, using only 25 MHz of signal bandwidth and 10 μ s of integration time, both of which are an order of magnitude less than passive microwave and millimeter-wave imaging systems.

Index Terms—Interferometric imaging, microwave imaging, millimeter-wave imaging, noise radar, radar imaging.

I. INTRODUCTION

MAGING systems in the microwave and millimeter-wave regions of the electromagnetic spectrum have gained significant interest in recent years for a wide range of applications, including contraband detection, security imaging, and medical imaging, among others. Favorable propagation characteristics in terrestrial environments, such as negligible attenuation when propagating through fog, smoke, dust, and other obscurants, as well as through clothing, baggage materials, and many wall materials, have been a major impetus for developing imagers and sensors in the 3-300-GHz range [1]-[3]. Furthermore, microwave and millimeter-wave technology is becoming increasingly more efficient and cost-effective, making the implementation and use of such imaging systems robust and affordable. Because of these reasons, imaging in the microwave and millimeter-wave frequencies is an emerging area, which holds significant potential for gaining new knowledge and developing new technologies. The field of microwave

Manuscript received May 1, 2018; revised July 17, 2018; accepted July 22, 2018. Date of publication September 10, 2018; date of current version December 11, 2018. This work was supported by the National Science Foundation under Grant 1708820. This paper is an expanded version from the 2018 International Microwave Symposium, Philadelphia, PA, USA, 10–15 June 2018. (Corresponding author: Jeffrey A. Nanzer.)

The authors are with the Department of Electrical and Computer Engineering, Michigan State University, East Lansing, MI 48824 USA (e-mail: nanzer@ieee.org).

Color versions of one or more of the figures in this paper are available online at http://ieeexplore.ieee.org.

Digital Object Identifier 10.1109/TMTT.2018.2867433

imaging is broad and active, and thus there exist many different technical approaches that have been developed in recent years. An exhaustive list is beyond the scope of this paper; in the following, we provide an overview of the major imaging methods that have been developed, followed by a discussion of the novel aspects that differentiates the work in this paper. The focus here is on microwave imaging approaches that provide images in the two angular domains (similar to an optical camera). Other forms of microwave imaging exist, notably tomographic imagers, such as synthetic aperture radar [4], inverse synthetic aperture radar [5], and medical tomographic imaging systems [6]; these methods obtain images across the range dimension and one angular dimension and are not considered here.

Scanning microwave imagers, where a narrow beam is scanned over a volume using either a mechanically gimbaled antenna such as a reflector antenna or a phased array, which electronically scans the beam, are among the most commonly implemented microwave imagers due to their relative simplicity of operation and concept [7], [8]. Multielement imaging systems come with a higher cost and system complexity than single-element ones and usually demand calibration for focusing the beam of phased arrays. However, their superior performance, faster operation, and resistance to failures outweighs their drawbacks. Ultrawideband scanning radars can be combined with quasi-optical components [9]-[12] for good resolution at millimeter-wave and submillimeter-wave bands. These systems can provide 3-D image reconstruction; however, they are generally complex and costly due to the very wide bandwidths required for fine range resolution. Scanning imagers furthermore can suffer from long image formation times and image shearing due to the need to physically scan a small beam over time.

Staring-type microwave imagers, such as focal plane arrays [13], and more recently introduced compressive imagers form images without the need for beam scanning; however, these approaches generally require quasi-optical apertures, such as lenses or reflector antennas, which lead to large and bulky systems. Computational imaging approaches, such as compressive imaging, also require dynamic masks, typically implemented on the largest aperture element, and furthermore necessitate high computational loads due to the complex image formation algorithms [14], [15]. Microwave and millimeter-wave holography techniques have been implemented [16]; however, these systems require long data acquisition time to produce high-resolution images along with multielement arrays and wide bandwidth.

Most of the above forms of microwave imaging require a large aperture that is fully or mostly filled, which for fine-resolution beams can result in large occupied areas and high cost. This requirement has recently led to interest in sparse array imagers, which sample the scene information in the spatial frequency domain rather than the spatial domain. Originally developed in radio astronomy, spatial frequency sampling imagers utilize sparse arrays [17], resulting in a significant reduction in the number of elements and aperture size and weight compared to other imaging techniques. Such imagers have been developed primarily for security imaging purposes due to the fact that the spatial frequency sampling image reconstruction method necessitates that the incident electromagnetic fields be spatially and temporally uncorrelated. Intrinsic thermal radiation generated by the human body (as well as the radiation from celestial bodies) satisfies this condition, and furthermore, human radiation is generally sufficiently greater than that of environmental objects to enable the detection of the shapes of objects hidden beneath a person's clothing, for example. Spatial frequency imagers operate very similarly to a simple CCD digital camera [18] or a focal plane array, in that no beam scanning or moving parts are necessary [19], although the image formation process requires cross correlations in signal processing. Furthermore, images degrade gracefully with element failures, since no one pixel corresponds to a single receiver; therefore, such imagers are a robust technology, which is resistant to failures, increasing the usable lifetime of the proposed millimeter-wave imagers [20].

A major drawback of passive spatial frequency imagers is that thermal radiation measured by such systems is exceedingly small at microwave and millimeter-wave frequencies (often on the order of femtowatts), necessitating receivers with extremely high sensitivity, which can only be achieved with systems that simultaneously have high gain, low noise, and wide bandwidth. Such receivers not only result in significant costs but are also challenging to appropriately calibrate; even small gain variations due to temperature variations in the amplifiers can cause considerable signal degradation. Therefore, it would be beneficial to use active transmitters in order to improve the signal-to-noise ratio and decrease the necessary sensitivity of the receivers; however, transmission of radar signals results in an appreciable amount of correlation on the scene in both space and time, thereby rendering the image reconstruction process invalid. The resulting effect from such signals is a significant amount of constructive and destructive interference from many reflecting points, effectively washing out the image information. As such, spatial frequency sampling generally cannot be implemented with current coherent or incoherent active approaches.

In this paper, we present a novel approach to microwave imaging that combines spatial frequency sampling with noise transmission similar to that used in noise radar techniques [21], [22]. By appropriately transmitting noise signals from multiple transmitters, the resulting radiation at the scene is sufficiently spatiotemporally incoherent that spatial frequency image reconstruction methods can be employed. The result is that active imaging approaches, which do not need the high-sensitivity, high-cost receivers of passive systems, can be implemented with a sparse aperture, significantly reducing the aperture size compared to other active microwave imaging approaches. The active incoherent microwave imaging

technique presented in this paper differs from other microwave imaging methods described above in a few significant ways, summarized by the following.

- It is simultaneously active (signal transmission is used to achieve high SNR) and staring (no beamsteering or beamforming is required), yielding snapshotlike images with no electrical or mechanical scanning. In comparison, other active imaging methods generally necessitate the formation of a narrow beam, with a quasi-optical system or a phased array, which must then be physically scanned over time.
- 2) It utilizes an aperture that is both planar and sparse, resulting in an easily implemented form factor with minimal antenna elements. Other staring imaging methods, such as focal plane arrays and compressive imagers, rely on filled, quasi-optical apertures, which are more bulky and extend volumetrically in three dimensions.
- 3) It is the first active spatial frequency imager; all other spatial frequency imagers have been passive, necessitating costly, high sensitivity receivers. The presented technique, in contrast, achieves sufficient sensitivity with receivers using relatively low gain and bandwidth, which can be implemented with much lower cost.

It should be noted that the presented imaging method is incoherent in two senses of the term: the transmitted signal is noiselike and incoherent across time and space, and the receiver does not coherently detect the transmitted signal.

Previously, we demonstrated a 4.95-GHz 1-D active incoherent imager [23]. In this paper, we describe in detail the theory behind the imaging method and demonstrate 1-D and 2-D experimental imagery using a 5.85-GHz imaging system. The 2-D system consists of three noise transmitters and an inverted T-shaped receiving array, with a 93% reduction in aperture area compared to a filled array. We demonstrate the technique by reconstructing simple reflecting scenes consisting of metal spheres.

II. SPATIAL FREQUENCY SAMPLING

A 2-D scene can be represented by the superposition of an infinite series of spatial sinusoidally varying signals of different spatial frequencies. Spatial frequency sampling imagers measure the information in a scene by capturing the electromagnetic information associated with specific spatial frequencies. In a spatial frequency sampling array, each antenna pair corresponds to a specific spatial frequency, and by correlating the received signals between the antennas in a pair, a sample of the spatial frequency information is obtained.

For a given antenna pair in the array observing a single point radiating source as shown in Fig. 1, the received signals can be given by [24]

$$V_1(t) = \cos(2\pi f t) + n_1(t) \tag{1}$$

$$V_2(t) = \cos[2\pi f(t - \tau_g)] + n_2(t) \tag{2}$$

where f is the carrier frequency, θ is the angle that the baseline forms with the point source, $\tau_g = (D/c) \sin \theta$ is the geometric time delay, which is the time difference the plane wavefront faces in reaching the two elements spaced D apart, c is the

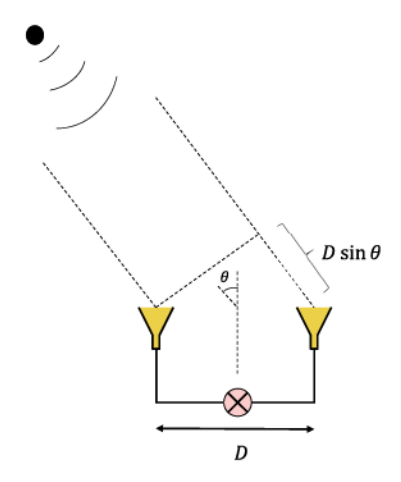


Fig. 1. Correlation interferometer observing a radiating point source.

speed the wavefront propagates, and n_i is the noise generated by the *i*th element. The two voltages are then multiplied and integrated. Because the signal voltage is uncorrelated from the noise components, and the noise components are uncorrelated with one another, the noise components will average to zero as integration time increases; this integration can be accomplished in hardware with a low-pass filter. The response of the correlation interferometer at the output of a low-pass filter can be given by

$$r(\theta) = \langle V_1 V_2 \rangle = \langle \cos(2\pi f t) \cos[2\pi f (t - \tau_g)] \rangle. \tag{3}$$

The low-pass filter will cut off the high carrier frequency, resulting in

$$r(\theta) = \frac{1}{2} \cos\left(\frac{2\pi}{\lambda} D \sin\theta\right) \tag{4}$$

where $\lambda = c/f$ is the corresponding wavelength. Thus, the output of the correlator is a sinusoidal response relative to $\sin \theta$. The result is a spatial receiving pattern that includes a number of grating lobes, depending on the length of the baseline, which defines a specific spatial frequency, whose units are cycles per radian. The information represented by (4) is thus the scene information in a single spatial frequency.

A. Visibility Sampling

If the antenna pair is observing a distributed source whose spatially distributed intensity is $I(\gamma)$, where $\gamma = \sin \theta$, the output of the antenna pair can be shown to be [24], [25]

$$r(\theta) = \frac{kA_e}{2\lambda^2}V(u) \tag{5}$$

where k is Boltzmann's constant, A_e is the mean effective area of the antennas, $u = D_{\lambda} = D/\lambda$ is the spatial frequency, which is equal to the baseline between the two antenna elements normalized to the wavelength of the center frequency, and

$$V(u) = \int_{-\infty}^{\infty} I(\gamma)K(\gamma)e^{j2\pi u\gamma}d\gamma \tag{6}$$

is the *visibility* of the scene, which resides in the spatial frequency domain. In the above, $K(\gamma)$ is the system beam pattern, which is the product of the antenna pattern and the

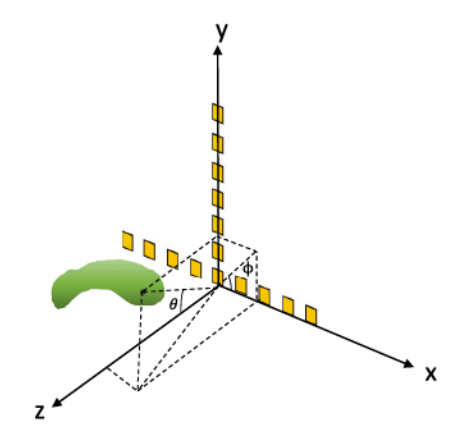


Fig. 2. 2-D antenna array observing a radiating source.

bandwidth pattern, the latter of which results from the finite bandwidth of the receiver. Provided that the reconstructed intensity (the scene intensity modified by the system beam pattern) $T_r(\gamma) = I(\gamma)K(\gamma)$ is spatiotemporally uncorrelated, and when the field of view is centered on broadside and is narrow ($\gamma^2 \ll 1$), it follows from the Van Cittert-Zernike theorem [26], [27] that the reconstructed intensity and the visibility are related through a Fourier transform by:

$$I_r(\gamma) = \int_{-\infty}^{\infty} V(u)e^{-j2\pi u\gamma} d\gamma.$$
 (7)

If the intensity is spatiotemporally uncorrelated, the mutual coherence function of a distant incoherent source is equal to its complex visibility, and the above equation holds. Therefore, with a sufficient number of visibility samples taken at different baselines, the scene intensity, modified by the system beam pattern, can be reconstructed.

In some radio astronomy applications, the visibility can be sampled continuously as a function of the normalized baseline, as indicated by the integral of (6), by moving an antenna continuously or by tracking a celestial object as the earth rotates, thereby continuously altering the projected baseline. However, in situations where the image must be constructed quickly, such antenna movement is impractical, and a discrete set of baselines is implemented, which sample the visibility at a discrete set of spatial frequencies. This discrete sampling can be represented in the above formulation through the use of a sampling function

$$S(u) = \sum_{n=0}^{N} \delta(u - u_n)$$
 (8)

where N is the number of baselines, or spatial frequencies, represented in the array. The reconstructed scene intensity is then given by

$$I_r(\gamma) = \sum_{n=1}^{N} V(u_n) e^{-j2\pi u_n \gamma}.$$
 (9)

The above extends directly to 2-D spatial frequency sampling and image reconstruction. The 2-D visibility is

given by

$$V(u,v) = \iint_{-\infty}^{\infty} I(\alpha,\beta)K(\alpha,\beta)e^{j2\pi(u\alpha+v\beta)}d\alpha d\beta \quad (10)$$

where $\alpha = \sin \theta \cos \phi$ and $\beta = \sin \theta \sin \phi$ are the direction cosines relative to u and v, as shown from the angles in Fig. 2. The 2-D reconstructed scene is then given by

$$I_r(\alpha, \beta) = \sum_{n=1}^{N} \sum_{m=1}^{M} V(u_n, v_m) e^{-j2\pi(u_n\alpha + v_m\beta)}.$$
 (11)

Prior work in spatial frequency sampling imaging has taken place with passive systems, because a necessary requirement for the image formation process is that the signal emanating from the scene is temporally and spatially incoherent. The thermally generated electromagnetic energy emitted from an object is spatially and temporally incoherent, and by computing the correlation integrals between each element pair, a sample of the source visibility is obtained. However, this is not true for active systems. For an active spatial frequency sampling system, it is necessary to transmit a signal that is temporally incoherent within the sampling interval and spatially incoherent within the resolution of the receiving array. For that purpose, we use independent noise generators as the transmission sources, which have random amplitude and phase noise.

Another assumption for the Van Cittert-Zernike theorem to work is that the distance between the source and the antenna array is larger than the far-field distance. In order to meet the far-field requirement, a central frequency in the microwave or millimeter-wave region is necessary for the distance between the scene and the antenna array to be easily larger than the far-field distance, and for the spacings between the array elements to be physically small. Also, because the array's resolution is dependent on its larger electrical dimension, higher frequencies are desirable in order to achieve a smaller and more compact imaging system with a better resolution [28]–[30]. In Section III, we analyze the statistical properties of the spatiotemporal transmit signal to ensure that the incoherence criterion is met.

B. Spatial-Domain Interpretation

It is instructive to consider the spatial frequency imaging process in the spatial domain as well. In the above-mentioned formulation, we describe the process in the spatial frequency domain: the visibility, being the Fourier transform of the scene intensity, resides in the spatial frequency domain and the sampled visibility is the product of the sampling function and the visibility. These also reside in the spatial frequency domain, and thus the last inverse Fourier transform (IFT) step converts the information back to the spatial domain. We can also look at the process in terms of the scene intensity, and the spatial-domain response of the sampling function, which is the point-spread function (PSF) of the array, where

$$PSF(\alpha, \beta) = IFT\{S(u, v)\}. \tag{12}$$

The PSF represents a synthesized beam in the spatial domain and is defined by the baselines included in the array. The output of the imaging process, the reconstructed image, is the convolution of the scene intensity and the PSF

$$I_r(\alpha, \beta) = PSF(\alpha, \beta) * I(\alpha, \beta)$$
 (13)

where * indicates convolution. From this formulation, it can be seen that the reconstructed image will be modified by the shape of the PSF. The ideal PSF is a delta function, i.e., $PSF(\alpha, \beta) = \delta(\alpha, \beta)$; however, in practice, it will consist of a main beam and a number of sidelobes of varying amplitudes.

III. TRANSMIT SIGNAL ANALYSIS FOR ACTIVE IMAGING

The use of the Van Cittert-Zernike theorem in spatial frequency imaging is based partly on the assumption that the signals received from the array elements are spatially incoherent. In the case where spatial coherence is present, for instance, if a single active transmitter emits a monochromatic signal, the Fourier inversion of the sampled visibility results in a series of cross terms that represent spatial constructive and destructive interference resulting from coherent signals reflecting off the various scattering centers in the scene. Even in cases with only a few scatterers, this can significantly degrade the image reconstruction process. It is, therefore, important for our active imaging technique that the signals are spatially and temporally incoherent.

To determine the spatiotemporal properties of the transmitted signals, we consider the case of a 1-D scene spanning $\theta \in (-(\pi/2), (\pi/2))$. The spatiotemporal transmit pattern of an array with L elements is given by

$$A(\theta, t) = \sum_{l=1}^{L} \left[e^{j[\omega t + \phi_l(t)]} + \omega_l(t) \right] e^{-jkd_l \sin \theta}$$
 (14)

where $w_l(t)$ is random amplitude noise and $\phi_l(t)$ is random phase noise. The random noise is necessary in order to achieve spatial and temporal incoherence. The factor $e^{j\omega t}$ is the sinusoidal input of each element representing the center frequency of the transmitted signals, and the $e^{-jkd_l\sin\theta}$ factor represents the additional time delay the wavefront faces in order to reach element l.

The spatiotemporal scene is proportional to the reflected radiation from the scene $s_r(\theta)$ and can be calculated from

$$s_{\rm st}(\theta, t) = A(\theta, t)s_r(\theta). \tag{15}$$

The received radiation of the *l*th element of the array can be expressed as a sum of the spatiotemporal scene over angle by

$$r(l,t) = \int_{-\frac{\pi}{4}}^{\frac{\pi}{2}} s_{\rm st}(\theta,t) e^{-jkd_l \sin \theta} d\theta.$$
 (16)

To adhere to the assumptions of the Van Cittert-Zernike theorem, the spatiotemporal scene must be sufficiently noise-like. Fig. 3 shows the spatiotemporal transmit pattern of a 31-element array with 1λ spacing. From Fig. 3, the signal in both space (horizontal axis) and time (vertical axis) appears to be noiselike; however, to analyze this property more concretely, we calculate the autocorrelation of the transmitted waveform, which is shown in Fig. 4. The autocorrelation displays a strong peak at (0, 0) with much lower amplitude

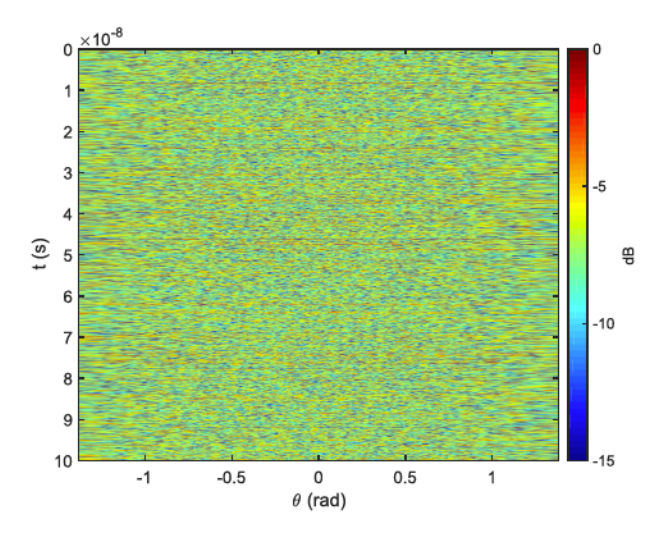


Fig. 3. Transmitted noise signal (normalized to 0 dBm) in the spatial domain (horizontal axis) and the temporal domain (vertical axis). The uncorrelated nature of the signal in both space and time is evident; however, the autocorrelation of the signal provides a more concrete metric for spatiotemporal incoherence.

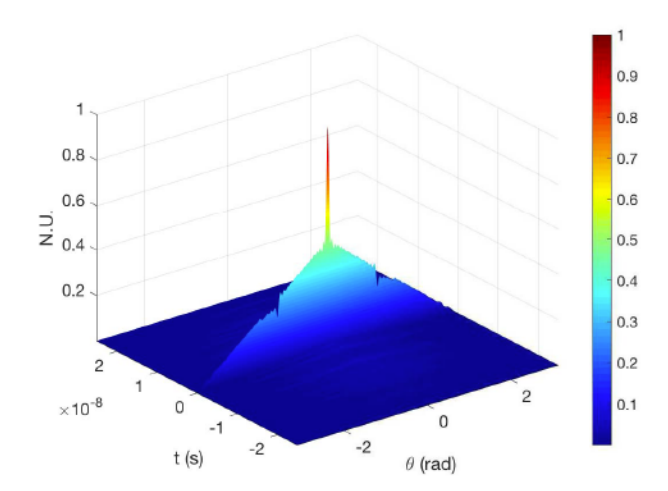


Fig. 4. 2-D autocorrelation of the spatiotemporal transmit pattern displays a strong response at (0,0) with lower response elsewhere, demonstrating that the signal is sufficiently uncorrelated in both time and space, thereby indicating the feasibility of its use for active spatial frequency sampling. The amplitude is normalized, and hence, the vertical axis is in normalized units (N.U.).

elsewhere, indicating that the transmitted signal is sufficiently uncorrelated in the spatiotemporal domain. The slightly raised area in the spatial domain (along the θ -axis) indicates that the signal is more correlated in the spatial domain than the temporal domain. This results from the transmit array having a comparatively wider bandwidth in the temporal domain than the spatial domain. While resulting in greater spatial correlation, this is not a problem for the imaging process as long as the receiving array does not have a wider spatial bandwidth than the transmitter. Another way of interpreting this is in regard to the resolution of the arrays: wider spatial bandwidth results in finer spatial resolution; therefore, as long as the transmitter has finer spatial resolution than the receiver, any spatial correlation will fall within a resolution bin in the reconstructed image, effectively enforcing the spatial incoherence

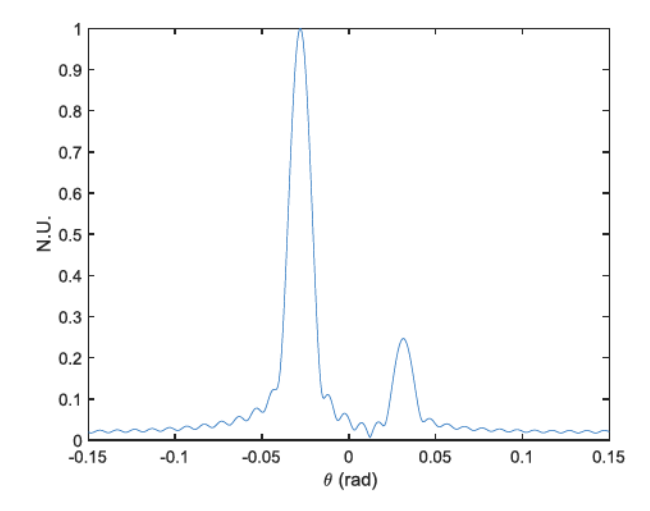


Fig. 5. Simulation of a 1-D dual-target reconstruction with two point objects of different reflectivities. The amplitude is normalized, and hence the vertical axis is in normalized units (N.U.).

requirement. In other words, using two transmitters spaced at an equal or greater separation than the widest element separation in the receiving array will ensure that the spatial variation of the transmitted signal is smaller than the resolution of the receiving array, and thus that the received signal is spatially incoherent, thereby satisfying the Van Cittert–Zernike theorem.

To reconstruct the image, the outputs of each antenna pair are then correlated, yielding a sample of the visibility, the basic quantity measured by interferometric imaging systems. Because a certain spatial frequency may correspond to more than one antenna pair, the redundant ones can be omitted. The IFT of the reconstructed visibility is the reconstructed scene in the spatial domain. Fig. 5 shows a simulation of a reconstructed scene using a 31-element 4.95-GHz array viewing a scene with two reflecting targets of different amplitudes at $\theta=\pm0.03$ rad and amplitude ratio of 5 to 1. The sampling frequency was twice the carrier frequency, and 3000 samples were used for the correlation.

IV. EXPERIMENTAL SETUP AND IMAGING RESULTS

Verification measurements of the active interferometric imaging method were carried out in a semienclosed antenna range, using metal spheres for targets. Two experiments were conducted: one implementing a linear array generating 1-D images and one implementing a 2-D array generating 2-D images. The overall measurement system is shown in Fig. 6 and consists of separate transmit and receive subsystems, each consisting of several antenna elements. The transmit signals were generated using a Keysight M8190 arbitrary waveform generator (AWG), which is capable of generating signals through the X-band with 14-bit resolution. The output power of the AWG was -9 dBm. The amplifiers each had a gain of 9 dB and a 1-dB compression point of 19 dBm. The transmit antennas were 20-dBi standard gain horn antennas. For the linear array, two transmit antennas were used, while for the 2-D array, three transmitters were used. The antennas were placed on a 7.3-m-diameter arch range, as shown in Fig. 7.

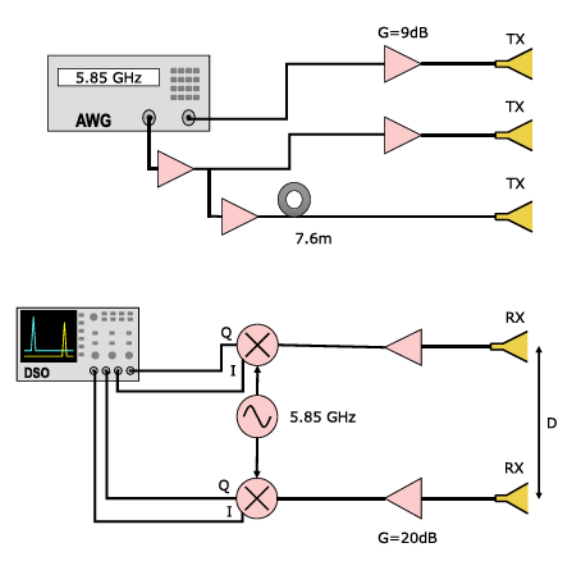


Fig. 6. Block diagram of the experimental imaging system. For the 1-D system, the third transmitter was not used. The distance *D* was changing in order to synthesize the 1-D or 2-D receiver array.

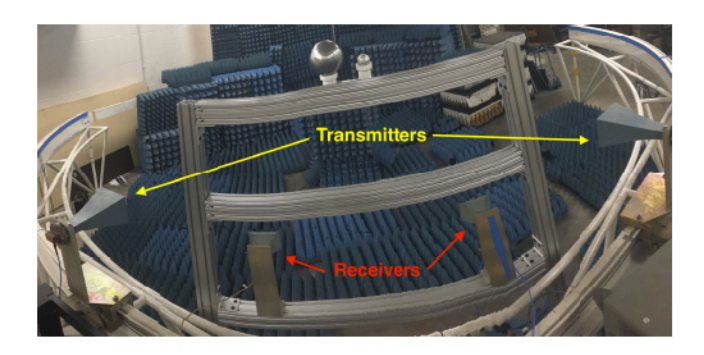


Fig. 7. Wide-angle image of the experimental setup for 1-D imaging. The transmit antennas are shown on either side of the image and the receive antennas are located on the rack. The two reflecting spheres that served as targets are seen in the antenna range near the top of the image.

The receiving array was synthesized using two receiving elements, which were placed pairwise in the appropriate locations to generate the desired sampling function. Synthesizing the array with a pair of sequentially moved antennas removed the need to calibrate a set of antenna elements, simplifying the proof-of-concept experiments. Since the signals are spatiotemporally incoherent and the information is sampled on a pairwise basis, synthesizing the array in this manner is valid. This synthesis approach was common in radio astronomical observations [31]. The receiving antennas were 10-dBi standard gain horn antennas placed on a metal rack with movable fixtures. Each received signal was input to a quadrature downconverting mixer (Analog Devices ADL5380). Because this system does not include filters, the mixers represent the band-limiting devices in the system. The bandwidth of the received signals was at least 390 MHz as specified by the passband of the mixers; however, without filters, some signals outside this band were present, in particular leakage from the mixer introduced spurious signals. Undersampling and digital low-pass filtering were used to mitigate these spurs. The received signals were captured using an oscilloscope and

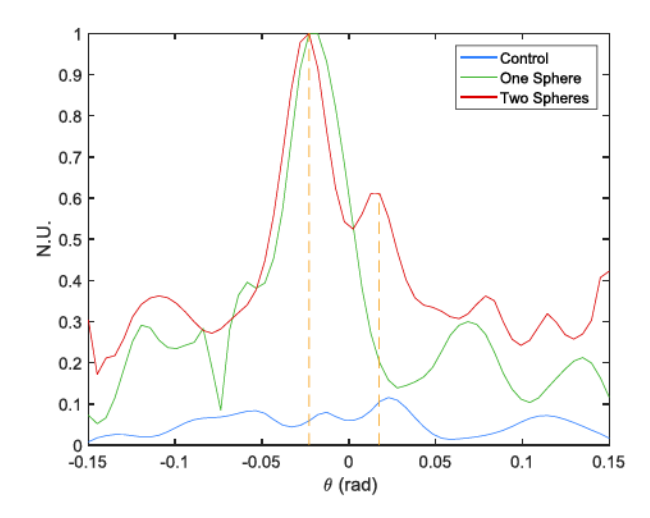


Fig. 8. 1-D reconstructed experimental scenes from an array with 1λ spacing between the elements, showing the control measurement (no target), a single reflecting target, and two reflecting targets.

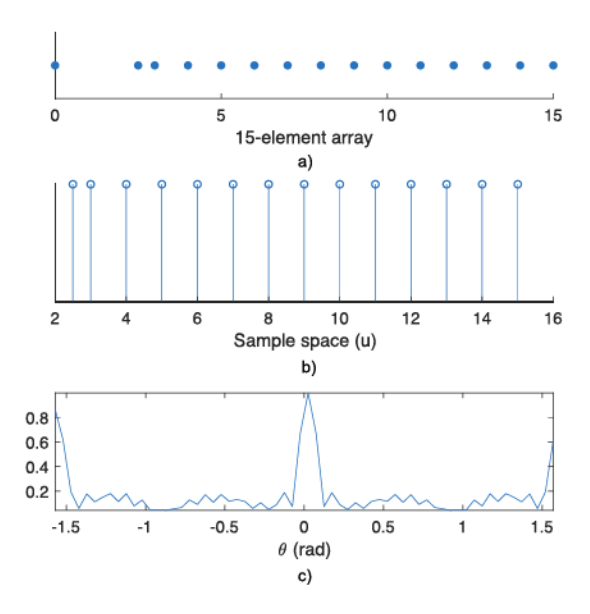


Fig. 9. Diagram of (a) element locations, (b) sampling function, and (c) normalized PSF of the 1-D linear array.

processed off line using MATLAB. Each signal was filtered to remove dc bias, and the output from each antenna location was cross correlated with every other antenna location, excepting redundant antenna baselines.

A. 1-D Imaging System and Experimental Measurements

Initial proof-of-concept measurements were conducted using a linear array. The transmitted noise waveforms were centered at 4.95 GHz with the characteristics of broadband white noise. The two transmitters produce a sufficient noiselike spatiotemporal transmit pattern similar to the one from the array in Fig. 3. The receiving array was synthesized by moving the placement of one of the receiver elements over a space of 15λ , synthesizing an array filled at the antenna spacings of 1λ . The resulting array had a sparsity of 50% compared to a traditional filled array with $(1/2)\lambda$ element spacing.

It should be noted that the minimum spacing measurement that took place was at 2.5λ because of the dimensions of the horn antennas used as receivers; however, above this spacing, the antennas were moved in increments of 1λ . The responses, after downconverted, were captured using a 4-channel oscilloscope, sampled at 50 MSa/s for 10240 samples.

Three experiments were conducted: one control test with no target present, one with a single reflecting target, and one with two reflecting targets. The reconstructed 1-D scenes are shown in Fig. 8. The larger response comes from a sphere with the radius of 18 cm, while the smaller response comes from a sphere with a radius of 8 cm, located in the top of Fig. 7. The two spherical targets were located at an angle of ± 0.02 rad, as shown in Fig. 7. It is clearly seen that the control scene produces no appreciable signal response, while the reconstructed scenes for a single and double target show one and two responses, respectively. While the target responses are clear, an increase in the noise floor is apparent outside of the target responses. This increase in noise results from the convolution of the PSF with the target scene. In comparison to the ideal simulations of Fig. 5, the noise outside of the signal responses is increased, which we attribute to additional system noise and measurement imperfections. The array layout is shown in Fig. 9, as well as the sampling function and the resulting PSF of the linear array. Sidelobes, although relatively low, are present in the PSF, and the presence of sidelobes contributed to signal energy outside of the target locations. This effect can be easily interpreted in the context of the image reconstruction consisting of the convolution of the PSF and the scene intensity.

B. 2-D Imaging System and Experimental Measurements

The interferometric imaging process extends directly to two dimensions, and similar to the 1-D case, the spatial frequency sampling process can be accomplished by sequentially moving the receiving antennas to the appropriate locations in a 2-D array. We simulated the 2-D response of a scene consisting of two point reflectors of different amplitudes, representing the two spheres in the measurement, using a 2-D array in the shape of an inverted T, as shown in Fig. 10. The gaps in the array locations were chosen to match those in the measurement system, where the smallest baselines were not achievable due to the physical size of the horn antennas. The result of losing the narrowest baselines in the array is a reduction in the low spatial frequency content in the image, which accounts for characteristics such as intensity in spatially broad areas. Edges and shapes are, however, still reconstructed well without such low spatial frequency content. For this simulation, the sampling function was calculated from the locations of the elements, and the reconstructed scene was calculated by multiplying the Fourier transform of the simulated scene and the sampling function. This simulation was parameterized as a function of spacings in terms of wavelength and simulated the spatial frequency sampling of the 2-D array. The Fourier transform of the output generates the simulated image, as shown in Fig. 11, where the two point targets, located at an azimuth angle of ± 0.05 rad, are visible

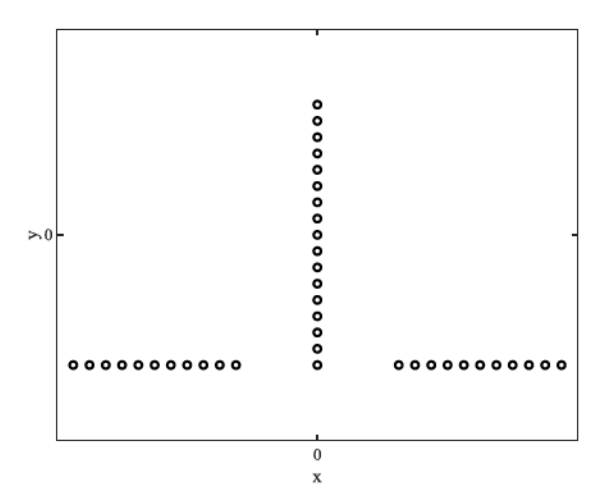


Fig. 10. Element locations for the 2-D imaging setup. Two antennas were used and moved sequentially until all antenna pairs were represented in the measurement, in $(\lambda/2)$ increments. For spatial frequency sampling, far fewer elements are necessary than in a traditional filled array. The smallest baselines were not achievable due to the physical size of horn antennas.

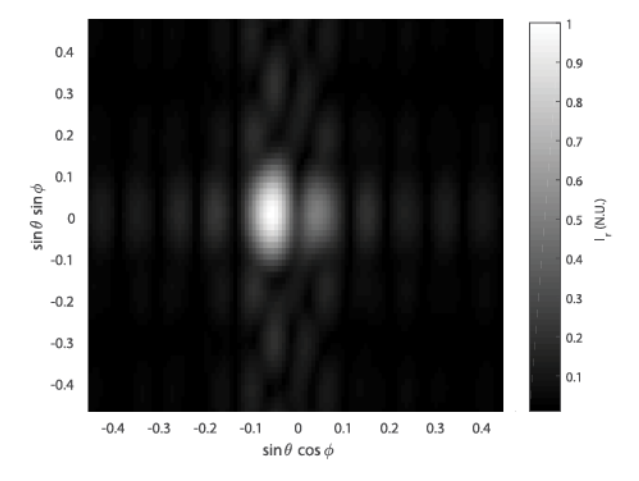


Fig. 11. Simulated 2-D dual-target reconstruction from a T-array. The ringing seen in the vertical and horizontal directions is due to the sidelobes in the PSF, which is convolved with the scene. The amplitude is normalized, and hence the color bar axis is in normalized units (N.U.).

at the center of the image. The stronger response comes from a spherical target with twice the radius of the smaller one. The sidelobe structures in the vertical and horizontal directions are again due to the sidelobes in the PSF.

For the 2-D experiment, the transmitted noise signals were centered at a carrier frequency of 5.85 GHz. Two spheres were placed in the center of the same 7.3-m-diameter antenna range, seen in Fig. 12. Three 20-dBi standard gain horn antennas were used for the transmitters in order to produce a sufficient noiselike transmit pattern in both the azimuth and elevation planes. It is necessary for the transmit signals to provide spatial incoherence in both dimensions, thereby requiring three antennas.

The Keysight M8190 AWG was again used to produce the noise signals; however, because only two independent outputs are available on the M8190, one of the outputs was split into two using a wideband splitter to generate two noise

TABLE I

Comparison of Bandwidth and Integration Time Between Passive Imaging and Active Incoherent Microwave Imaging

	[32]	[33]	[34]	[35]	[36]	[37]	This work
Bandwidth	10 GHz	7 GHz	200 MHz	1 GHz per pixel	40 GHz	20 GHz	25 MHz
Integration time	100 ms	3 s	1 ms to 1 s	30 ms per pixel	1 ms per pixel	2.5 ms per pixel	10 μs



Fig. 12. Two reflecting spherical targets used as the 2-D scene.

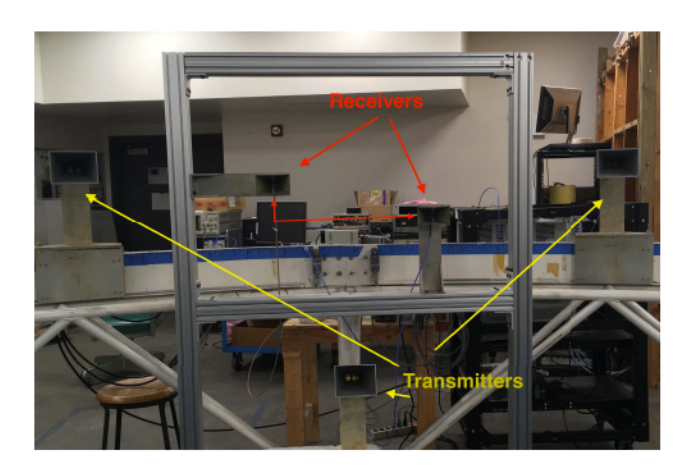


Fig. 13. Configuration for the 2-D experimental measurements with three noise transmitters and two receivers. The transmitter locations were not moved, while the receiving antennas were sequentially moved to the locations in an inverted-T array.

signals. One output of the splitter was connected to one transmitter, while the other output was connected to the second transmitter through a 7.6-m cable (see Fig. 6). This additional delay ensured that the transmitted signals were temporally uncorrelated when the signals were incident on the scene. In practice, separate noise transmitters would be preferable. An additional 9-dB gain amplifier with a 1-dB compression point of 19 dBm was used to overcome the losses from the splitter and the 7.6-m cable.

The synthesized array was an inverse T-array with elements placed in the locations indicated in Fig. 10 using the rack in Fig. 13 and the two receiver antennas. By moving the one in the horizontal and the other in the vertical direction,

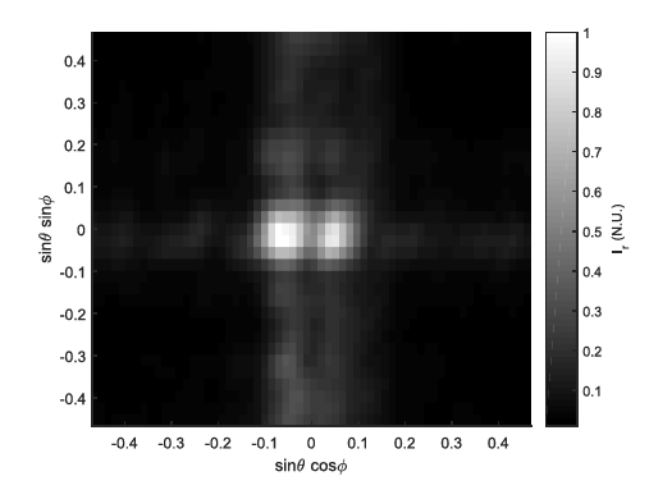


Fig. 14. Reconstructed 2-D image from a T-array with 0.5λ minimum spacing between the elements in grayscale format. The amplitude is normalized, and hence the colorbar axis is in normalized units (N.U.).

the T-array was synthesized with a maximum spacing of 15λ in the horizontal axis and 8λ in the vertical axis, and a minimum spacing of 0.5λ . The two received signals were amplified with 20-dB low-noise amplifiers, downconverted using the same quadrature mixers as in the 1-D imaging setup, and then captured using the 20-GHz MSOX92004A oscilloscope in the high-resolution mode. The captured files were processed off line using MATLAB, where they were low-pass filtered to a bandwidth of 25 MHz, dc bias was removed, and cross correlation was applied to each antenna pair, ignoring the redundant baselines. The integration time was 10 μ s. Both the bandwidth and the integration time are significantly lower than what is typically used in passive microwave and millimeter-wave imagers, where wide bandwidth and long integration times are required to overcome the minimal signalto-noise ratio resulting from the very low radiated thermal electromagnetic signals. Table I presents a comparison of these parameters for the proposed system and some well-known and recent passive imagers from the literature, showing that the proposed system obtains 2-D images with an order of magnitude reduction in both bandwidth and integration time.

Fig. 14 shows the reconstructed 2-D image of the two reflecting spheres. The two spheres were located at an azimuth angle of ± 0.05 rad; the stronger response comes from the sphere shown in the left-hand side of Fig. 12, which has a radius of 18 cm, while the weaker response comes from the sphere on the right with the radius of 12 cm. After the IFT was applied to the sampled visibility, a Gaussian smoothing filter was applied. The responses from the two spheres are clearly

evident, along with some minor signal energy outside of the target responses, which is again due to the sidelobe structure in the PSF. The strong match between the measured 2-D images compared to the simulated image of Fig. 11 demonstrates the feasibility of the active interferometric imaging method.

V. CONCLUSION

A novel active microwave imaging method has been demonstrated using noise transmitters and a spatial frequency sampling array. Measurements of simple 1-D and 2-D scenes were taken to demonstrate the ability to use an active system combined with spatial frequency sampling to generate microwave images. While measurements were conducted at carrier frequencies below 6 GHz, the experimental results show potential for a range of promising applications, including contraband detection, search and rescue operations, security sensing, medical imaging, and others.

Measurements in the presented system were conducted by synthesizing a larger array using a set of antennas sequentially moved in space. Because the signals received by the array were spatially and temporally incoherent, this approach is valid. In practical antenna arrays, there may arise issues with mutual coupling, which are not represented in this paper. However, we note that the synthesized array for the presented technique is sparse with a significantly smaller number of adjacent elements than a traditional filled array, and thus the impact of mutual coupling is likely to be small. Future implementations using simultaneous receiving array measurements may enable fast imaging capabilities. Since the received signal power can be influenced using the transmitters, the imaging time can potentially be reduced compared with passive imagers, where sensitivity increases require additional integration time or bandwidth.

REFERENCES

- E. J. Bond, X. Li, S. C. Hagness, and B. D. Van Veen, "Microwave imaging via space-time beamforming for early detection of breast cancer," *IEEE Trans. Antennas Propag.*, vol. 51, no. 8, pp. 1690–1705, Aug. 2003.
- [2] N. K. Nikolova, "Microwave imaging for breast cancer," *IEEE Microw. Mag.*, vol. 12, no. 7, pp. 78–94, Dec. 2011.
- [3] J. A. Nanzer, "A review of microwave wireless techniques for human presence detection and classification," *IEEE Trans. Microw. Theory Techn.*, vol. 65, no. 5, pp. 1780–1794, May 2017.
- [4] A. Moreira, P. Prats-Iraola, M. Younis, G. Krieger, I. Hajnsek, and K. P. Papathanassiou, "A tutorial on synthetic aperture radar," *IEEE Geosci. Remote Sens. Mag.*, vol. 1, no. 1, pp. 6–43, Mar. 2013.
- [5] L. Zhang, Z.-J. Qiao, M.-D. Xing, J.-L. Sheng, R. Guo, and Z. Bao, "High-resolution ISAR imaging by exploiting sparse apertures," *IEEE Trans. Antennas Propag.*, vol. 60, no. 2, pp. 997–1008, Feb. 2012.
- [6] M. Bassi, M. Caruso, M. S. Khan, A. Bevilacqua, A. Capobianco, and A. Neviani, "An integrated microwave imaging radar with planar antennas for breast cancer detection," *IEEE Trans. Microw. Theory Techn.*, vol. 61, no. 5, pp. 2108–2118, May 2013.
- [7] A. Clemente, L. Dussopt, R. Sauleau, P. Potier, and P. Pouliguen, "Wideband 400-element electronically reconfigurable transmitarray in X band," *IEEE Trans. Antennas Propag.*, vol. 61, no. 10, pp. 5017–5027, Oct. 2013.
- [8] S. S. Ahmed, A. Schiessl, and L.-P. Schmidt, "A novel fully electronic active real-time imager based on a planar multistatic sparse array," *IEEE Trans. Microw. Theory Techn.*, vol. 59, no. 12, pp. 3567–3576, Dec. 2011.

- [9] G. Rubio-Cidre, A. Badolato, L. Úbeda-Medina, J. Grajal, B. Mencia-Oliva, and B.-P. Dorta-Naranjo, "DDS-based signalgeneration architecture comparison for an imaging radar at 300 GHz," *IEEE Trans. Instrum. Meas.*, vol. 64, no. 11, pp. 3085–3098, Nov. 2015
- [10] D. A. Robertson et al., "340-GHz 3D radar imaging test bed with 10-Hz frame rate," Proc. SPIE, vol. 8362, pp. 836206-1–836206-11, May 2012.
- [11] K. B. Cooper et al., "Penetrating 3-D imaging at 4- and 25-m range using a submillimeter-wave radar," *IEEE Trans. Microw. Theory Techn.*, vol. 56, no. 12, pp. 2771–2778, Dec. 2008.
- [12] L. Carrer and A. G. Yarovoy, "Concealed weapon detection using UWB 3-D radar imaging and automatic target recognition," in *Proc. 8th Eur. Conf. Antennas Propag. (EuCAP)*, Apr. 2014, pp. 2786–2790.
- [13] D. A. Scribner, M. R. Kruer, and J. M. Killiany, "Infrared focal plane array technology," *Proc. IEEE*, vol. 79, no. 1, pp. 66–85, Jan. 1991.
- [14] F. Krahmer and R. Ward, "Stable and robust sampling strategies for compressive imaging," *IEEE Trans. Image Process.*, vol. 23, no. 2, pp. 612–622, Feb. 2014.
- [15] J. Hunt et al., "Metamaterial apertures for computational imaging," Science, vol. 339, no. 6117, pp. 310–313, Jan. 2013.
- [16] D. M. Sheen, D. L. McMakin, and T. E. Hall, "Three-dimensional millimeter-wave imaging for concealed weapon detection," *IEEE Trans. Microw. Theory Techn.*, vol. 49, no. 9, pp. 1581–1592, Sep. 2001.
- [17] A. Moffet, "Minimum-redundancy linear arrays," *IEEE Trans. Antennas Propag.*, vol. AP-16, no. 2, pp. 172–175, Mar. 1968.
- [18] L. Yujiri, M. Shoucri, and P. Moffa, "Passive millimeter wave imaging," IEEE Microw. Mag., vol. 4, no. 3, pp. 39–50, Sep. 2003.
- [19] G. Krieger, "MIMO-SAR: Opportunities and pitfalls," IEEE Trans. Geosci. Remote Sens., vol. 52, no. 5, pp. 2628–2645, May 2014.
- [20] R. M. Hjellming, "The design of aperture synthesis arrays," in Synthesis Imaging in Radio Astronomy (Astronomical Society of the Pacific Conference Series), vol. 6, R. A. Perley, F. R. Schwab, and A. H. Bridle, Eds. San Francisco, CA, USA: Astronom. Soc. Pacific, 1989, p. 477.
- [21] R. M. Narayanan and M. Dawood, "Doppler estimation using a coherent ultrawide-band random noise radar," *IEEE Trans. Antennas Propag.*, vol. 48, no. 6, pp. 868–878, Jun. 2000.
- [22] R. M. Narayanan, "Through-wall radar imaging using UWB noise waveforms," J. Franklin Inst., vol. 345, no. 6, pp. 659–678, Sep. 2008.
- [23] S. Vakalis and J. A. Nanzer, "An active microwave imaging technique using spatial frequency sampling," in *IEEE MTT-S Int. Microw. Symp. Dig.*, Jun. 2018, pp. 816–818.
- [24] J. A. Nanzer, Microwave and Millimeter-Wave Remote Sensing for Security Applications. Norwood, MA, USA: Artech House, 2012.
- [25] J. A. Nanzer, "Millimeter-wave interferometric imaging sensors," in Proc. IEEE SENSORS, Nov. 2013, pp. 1–4.
- [26] A. R. Thompson, J. M. Moran, and G. W. Swenson, Jr., Interferometry and Synthesis in Radio Astronomy. Hoboken, NJ, USA: Wiley, 2001.
- [27] M. Born and E. Wolf, Principles of Optics. Cambridge, U.K.: Cambridge Univ. Press, 1999.
- [28] R. Appleby and R. N. Anderton, "Millimeter-wave and submillimeter-wave imaging for security and surveillance," *Proc. IEEE*, vol. 95, no. 8, pp. 1683–1690, Aug. 2007.
- [29] N. Sarmah et al., "A fully integrated 240-GHz direct-conversion quadrature transmitter and receiver chipset in SiGe technology," *IEEE Trans. Microw. Theory Techn.*, vol. 64, no. 2, pp. 562–574, Feb. 2016.
- [30] J. J. Lynch et al., "Passive millimeter-wave imaging module with preamplified zero-bias detection," *IEEE Trans. Microw. Theory Techn.*, vol. 56, no. 7, pp. 1592–1600, Jul. 2008.
- [31] W. N. Christiansen and J. A. Hogbom, *Radiotelescopes*. Cambridge, U.K.: Cambridge Univ. Press, 1969.
- [32] L. Yujiri et al., "Passive millimeter-wave camera," Proc. SPIE, vol. 3064, pp. 3064–3068, Jun. 1997.
- [33] J. Drewes and R. P. Daly, "Design of a high-resolution passive millimeter-wavelength camera for security applications," *Proc. SPIE*, vol. 7309, pp. 7309–7312, Apr. 2009.
- [34] H. Nohmi, S. Ohnishi, and O. Kujubu, "Passive millimeter-wave camera with interferometric processing," *Proc. SPIE*, vol. 6548, pp. 65480C-1–65480C-8, May 2007.
- [35] V. M. Patel and J. N. Mait, "Passive millimeter-wave imaging with extended depth of field and sparse data," in *Proc. IEEE Int. Conf. Acoust., Speech Signal Process. (ICASSP)*, Mar. 2012, pp. 2521–2524.

- [36] D. Becker et al., "A 350-GHz high-resolution high-sensitivity passive video imaging system," Proc. SPIE, vol. 7670, pp. 76700M-1–76700M-7, Apr. 2010.
- [37] H. Isiker, I. Ünal, M. Tekbas, and C. Özdemir, "An auto-classification procedure for concealed weapon detection in millimeter-wave radiometric imaging systems," *Microw. Opt. Technol. Lett.*, vol. 60, no. 3, pp. 583–594, Mar. 2018.



Stavros Vakalis (S'18) received the B.S. degree in electrical and computer engineering from the National Technical University of Athens, Athens, Greece, in 2017. He is currently pursuing the Ph.D. degree in electrical engineering at Michigan State University, East Lansing, MI, USA.

His current research interests include wireless microwave and millimeter-wave systems, antenna arrays, radars, and signal processing.



Jeffrey A. Nanzer (S'02-M'08-SM'14) received the B.S. degrees in electrical engineering and in computer engineering from Michigan State University, East Lansing, MI, USA, in 2003, and the M.S. and Ph.D. degrees in electrical engineering from The University of Texas at Austin, Austin, TX, USA, in 2005 and 2008, respectively.

From 2008 to 2009, he was a Post-Doctoral Fellow with Applied Research Laboratories, University of Texas at Austin, where he was involved in designing electrically small HF antennas and communication

systems. From 2009 to 2016, he was with The Johns Hopkins University Applied Physics Laboratory, Laurel, MD, USA, where he created and led the Advanced Microwave and Millimeter-Wave Technology Section. In 2016, he joined the Department of Electrical and Computer Engineering, Michigan State University, where he is currently a Dennis P. Nyquist Assistant Professor. He has authored or co-authored more than 80 refereed journal and conference papers, authored Microwave and Millimeter-Wave Remote Sensing for Security Applications (Artech House, 2012), and co-authored the chapter "Photonics-Enabled Millimeter-Wave Wireless Systems" in Wireless Transceiver Circuits (Taylor & Francis, 2015). His current research interests include distributed arrays, radar and remote sensing, antennas, electromagnetics, and microwave photonics.

Dr. Nanzer is a member of the IEEE Antennas and Propagation Standards Committee, the AP-S Education Committee, and the USNC/URSI Commission B. He was a founding member and the First Treasurer of the IEEE AP-S/MTT-S Central Texas Chapter. He was a recipient of the NSF CAREER Award in 2018, the DARPA Young Faculty Award in 2017, JHU/APL Special Achievement Awards in 2014 and 2016, and the JHU/APL Outstanding Professional Book Award in 2012. From 2013 to 2015, he served as the Vice-Chair of the IEEE Antenna Standards Committee. From 2016 to 2018, he was the Chair of the Microwave Systems Technical Committee (MTT-16), IEEE Microwave Theory and Techniques Society. He is currently an Associate Editor of the IEEE TRANSACTIONS ON ANTENNAS AND PROPAGATION.